Immobilizing single atom on high-entropy oxides as separator regulators for catalyzing low-temperature lithium-sulfur battery

Fei Na [a,1], Xiang Li [b,1], Jian Wang [c,d,f,**], Xiaomin Cheng [c], Jing Zhang [e], Yanli Wang [a,*], Hongzhen Lin [c], Liang Zhan [a], Licheng Ling [a], Yongzheng Zhang [a,*]

[a] State Key Laboratory of Green Chemical Engineering and Industrial Catalysis, State Key Laboratory of Chemical Engineering, Key Laboratory of Specially Functional Polymeric Materials and Related Technology (Ministry of Education), Shanghai Key Laboratory of Multiphase Materials Chemical Engineering, East China University of Science and Technology, Shanghai 200237, China
[b] Anhui Provincial Key Laboratory of Green Carbon Chemistry, Fuyang Normal University, Fuyang 236037, PR China
[c] i-Lab & CAS Key Laboratory of Nanophotonic Materials and Device, Suzhou Institute of Nano-Tech and Nano-Bionics, Chinese Academy of Sciences, Suzhou 215123, China
[d] Helmholtz Institute Ulm (HIU), Ulm D89081, Germany
[e] School of Materials Science and Engineering, Xi'an University of Technology, Xi'an 710048, China
[f] Karlsruhe Institute of Technology (KIT), Karlsruhe D76021, Germany

Keywords:
Lithium-sulfur battery
Sulfur redox kinetics
Single atom catalysts
High-entropy oxide
Desolvation barrier

A B S T R A C T

The commercialization of lithium-sulfur batteries suffers from severe polysulfide shuttling, the sluggish kinetics of sulfur redox reaction and large desolvation barrier. Herein, an atom-dispersed Fe immobilized on high-entropy oxides (Cu-Zn-Al-Ce-ZrO) (SA-Fe/HEO@NC) is proposed via electron delocalization engineering, which serves as an efficient separator regulator for catalyzing sulfur cascade redox reactions with enhanced desolvation kinetics This design leverages electron delocalization engineering to enhance sulfur cascade redox reactions and desolvation kinetics, as confirmed by theoretical simulations and comprehensive electrochemical characterizations, including time-of-flight secondary ion mass spectroscopy (TOF-SIMS) and *in-situ* Raman spectroscopy. Consequently, the cell with SA-Fe/HEO@NC modified separator displays final capacity of 1035 mAh g^{-1} at 0.2 C after 100 cycles, and stabilizes for 4.1 mAh cm^{-2} when increasing areal loading to ~6 mg cm^{-2} at 0.1 C after 200 cycles. Under 0 °C, an outstanding specific capacity of 751 mAh g^{-1} with the high capacity-retention of 78.3 % after 100 cycles is still achieved at 1 C, verifying the feasibility of integrating single atom catalyst on high-entropy compounds for rapid conversion kinetics.

1. Introduction

To meet the demand for high energy density and cost-effective rechargeable batteries, lithium-sulfur (Li-S) batteries are regarded as one of the most promising candidates because of their high capacity and abundant sulfur reserves [1]. However, the practical application of Li-S batteries still encounters some fundamental hurdles, including the dissolution of lithium polysulfides (LiPSs), the "shuttle effect" of LiPSs, the sluggish sulfur reaction kinetics and the large desolvation barrier, significantly degrading their capacity and cycle life [2–4]. To address these issues, researchers have made great efforts by employing various electrocatalysts. For example, carbon-based materials exhibit excellent conductivity and adsorption properties but suffer from limited catalytic activity, resulting in relatively poor long-cycle stability [5]. Metal oxides demonstrate strong catalytic capabilities but are hindered by poor conductivity, obtaining unsatisfactory rate capability [6]. Heterostructures offer remarkable synergistic effects, yet their synthesis conditions are harsh, limiting their large-scale application [7]. Single-atom catalysts (SACs) possess high atomic utilization efficiency, tunable electronic structures, and exceptional catalytic activity, however, achieving uniform distribution and high durability one remains challenging due to the lack of suitable catalyst carriers [8–10].

* Corresponding authors.
** Corresponding author at: i-Lab & CAS Key Laboratory of Nanophotonic Materials and Device, Suzhou Institute of Nano-Tech and Nano-Bionics, Chinese Academy of Sciences, Suzhou 215123, China.
E-mail addresses: wangjian2014@sinano.ac.cn, jian.wang@kit.edu (J. Wang), ylwang@ecust.edu.cn (Y. Wang), zhangyongzheng@ecust.edu.cn (Y. Zhang).
[1] These authors contributed equally to this work.

Recently, high-entropy materials have attracted increasing attention as catalysts in Li-S batteries due to their typical “cocktail effect”. According to the configurational entropy formula $S = R\ \ln N$ (where R is the gas constant and N is the number of components), the configurational entropy for high-entropy material is usually satisfying $S>1.5R$, indicating five or more uniformly dispersed metal cations in near-equimolar ratios are involved. In contrast, medium-entropy materials are typically composed of three to four main elements with a S value ranging from $1.0R$ to $1.5R$ [11–15]. The versatile elemental composition not only affords high-entropy materials with abandant adsorption and catalytic sites for sulfur species, but also induce intrinsic tensile strain to make it an ideal support to contribute to the stable dispersion of single

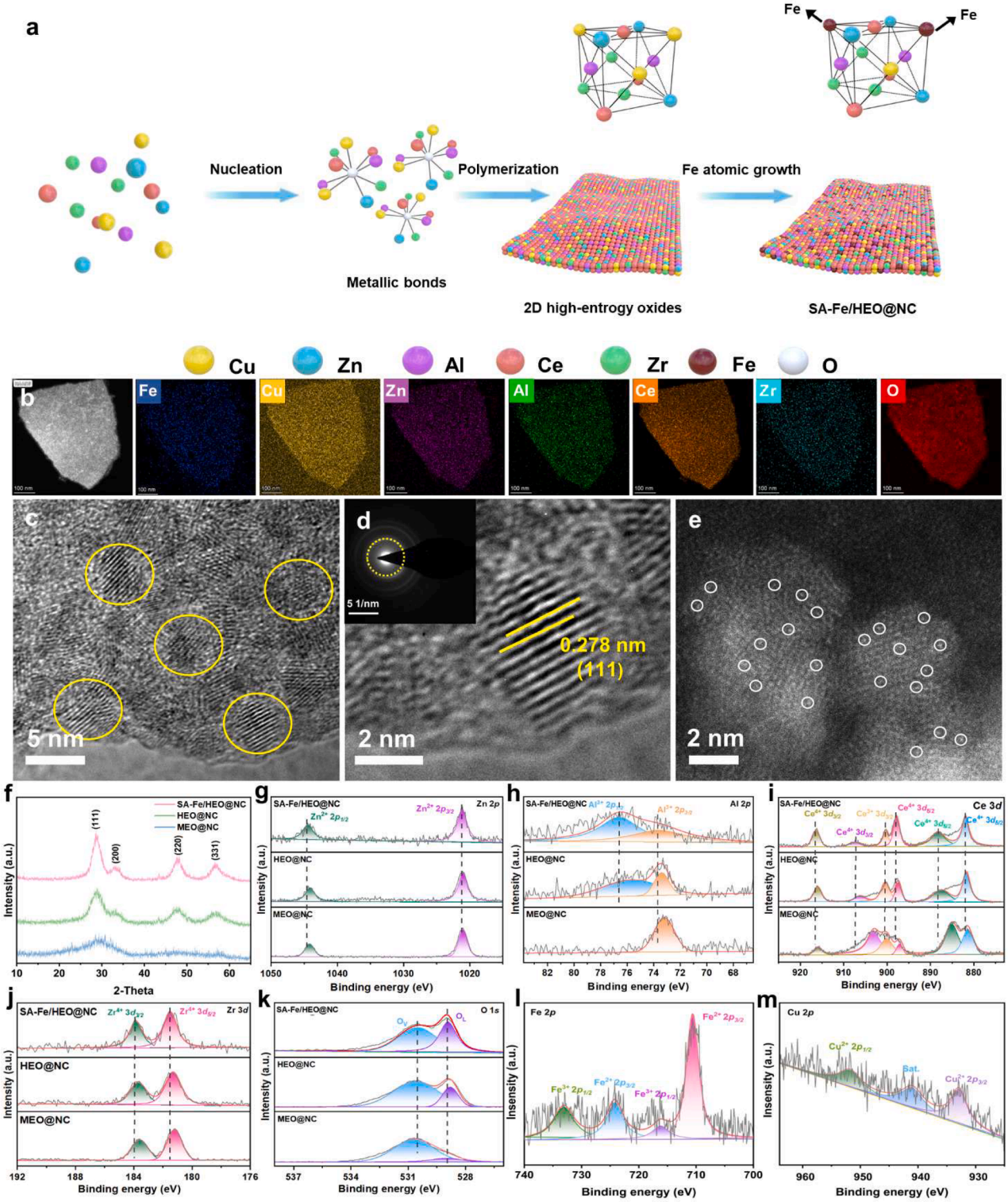

Fig. 1. a) Schematic illustration of SA-Fe/HEO@NC synthesis. b) HAADF-STEM image and corresponding EDS element mapping of SA-Fe/HEO@NC. c) TEM image and d) Lattice fringes of SA-Fe/HEO@NC. Inset is the SAED pattern. e) AC-TEM image of SA-Fe/HEO@NC. f) XRD spectrum. High-resolution XPS of SA-Fe/HEO@NC g) Zn 2p, h) Al 2p, i) Ce 3d, j) Zr 3d, k) O 1 s, l) Fe 2p and m) Cu 2p.

atom catalysts, further enhancing the overall catalytic performance. For example, when the nano high-entropy alloys catalyst was employed in Li-S batteries, the conversion activity of sulfur species was increased by 17 times [16–19]. The integration of Mo metal atoms with a high-entropy alloy notably improved the electrocatalytic performance for methanol oxidation, while simultaneously enhancing their chemical stability and service durability [20–22]. Nevertheless, the explorations of sulfur redox electrocatalysts that incorporate both single-atom and high-entropy composite remains lack and whether the catalysts have the effect on the interfacial desolvation kinetics is uncertain. More importantly, their catalytic mechanisms underlying Li-S battery remain unclear and require further comprehensive investigation.

Herein, atomic-level Fe immobilized on ultrasmall Cu-Zn-Al-Ce-ZrO high-entropy oxides is pioneered and developed on porous carbon (SA-Fe/HEO@NC), serving as the cascade catalyst for interfacial desolvation and sulfur redox reactions. Unlike conventional catalysts, SA-Fe/HEO@NC integrates the advantages of high-entropy oxides (HEOs) and single-atom Fe sites, providing enhanced catalytic activity and stability for interfacial desolvation and redox kinetics of sulfur species, as revealed by comprehensive characterization including electrochemical methods, *in-situ* Raman spectroscopy as well as theoretical simulations have revealed to promote the interfacial desolvation and redox kinetics of sulfur species, which is attributed to the catalytic behaviors of SA-Fe/HEO@NC. Thus, the Li-S batteries based on SA-Fe/HEO@NC modified separator obtains an excellent specific capacity (1035 mAh g^{-1} at 0.2 C). Despite a high sulfur loading over 6.0 mg cm^{-2}, a stable areal capacity of 4.1 mAh cm^{-2} was kept after 200 cycles at 0.1 C. Even under harsh conditions of 0 °C, the capacity-retention is 78.3 % at 0.1 C after 100 cycles, suggesting the potential for practical application.

2. Results and discussion

The SA-Fe/HEO@NC is synthesized through a simple pyrolysis impregnation strategy (Fig. 1a). Energy dispersive spectroscopy (EDS) elemental mapping in Fig. 1b indicate the coexistence and homogeneous distribution of Cu, Zn, Al, Ce, Zr, O, and Fe in the SA-Fe/HEO@NC. Scanning electron microscopy (SEM) (**Fig. S1**) and transmission electron microscopy (TEM) (**Fig. S2**) confirmed the 2D morphology of SA-Fe/HEO@NC. Fig. 1c depicts clearly visible lattice fringe of 0.278 nm (Fig. 1d), corresponding to the (111) crystal cubic (FCC) structure. The bright spots on HEO@NC demonstrated the successful construction of atomic Fe in SA-Fe/HEO@NC (Fig. 1e). Then, X-ray diffractions (XRD) of SA-Fe/HEO@NC reveals four peaks located near 29.4°, 33.7°, 48.2°, and 57.2°, corresponding to the (111), (200), (220), and (311) crystal planes of single cubic fluorite phase (Fig. 1f) [23,24]. Besides, no characteristic peaks of Fe are detected, suggesting the absence of Fe particles/clusters in the SA-Fe/HEO@NC. **Fig. S3** indicates that all six metal elements are detected on the SA-Fe/HEO@NC catalyst. The Zn 2p spectra (Fig. 1 g) shows typical double peaks at 1044.5 and 1021.1 eV, corresponding to Zn $2p_{1/2}$ and Zn $2p_{3/2}$ [25]. Compared to HEO@NC and MEO@NC, the peaks of Zn $2p_{1/2}$ in SA-Fe/HEO@NC shifts to 0.4 and 0.3 eV, respectively. Similar peak shifts were also observed in Al $2p_{1/2}$ (76.6 eV) and Al $2p_{3/2}$ (73.6 eV), Ce $3d_{5/2}$ (888.2 eV) and Ce $3d_{3/2}$ (907.5 eV) and Zr $3d_{5/2}$ and Zr $3d_{3/2}$ in the SA-Fe/HEO@NC compared to HEO@NC and MEO@NC. (Fig. 1h–1j) [26–29]. The O 1 s peak spectra (Fig. 1k) shows two obvious peaks at 530.5 and 528.9 eV, corresponding to the vacancy and lattice oxygen [30]. Notably, the binding energy of O_V in SA-Fe/HEO@NC shows a negative shift from 528.9 to 528.8 eV compared to that of HEO@NC and MEO@NC, indicating a stronger interfacial coupling between Fe and HEO@NC [31]. The Fe 2p spectra (Fig. 1l) shows four peaks at 716.2, 710.6, 724.2 and 733.1 eV, which was assigned to the Fe $2p_{3/2}$ orbitals of Fe^{2+} and Fe^{3+}, as well as the $2p_{1/2}$ band with Fe^{2+} and Fe^{3+} species, respectively [32]. The Cu 2p peak spectra (Fig. 1m) displays two peaks at 951.8 and 932.9 eV, corresponding to Cu $2p_{1/2}$ and Cu $2p_{3/2}$ [33]. To confirm the state of iron atom in SA-Fe/HEO@NC, X-ray absorption near-edge structure (XANES) spectroscopy analysis was conducted. The Fe K-edge XANES spectra, as shown in **Fig. S4**, revealed that the absorption edge position of SA-Fe/HEO@NC lies between the 0 and +3 oxidation states [34]. The extended X-ray absorption fine structure (EXAFS) spectra in R-space of the main peak of SA-Fe/HEO@NC further confirmed the atomic dispersion of Fe species anchored on HEO@NC. According to the ICP-OES result of SA-Fe/HEO@NC, the atomic ratios of Cu/Zn/Al/Ce/Zr are 19/26/16/25/14, and the Fe content is 0.53wt %. The TGA in **Fig. S5** shows the mass content of metal oxides is 48.57 %, which provides abundant catalytic sites for sulfur chemistry.

Subsequently, Raman spectra and a series of kinetic experiments were conducted to investigate the desolvation and ion diffusion behaviors catalyzed by SA-Fe/HEO@NC [35]. When large-sized solvated Li^+ passes through the SA-Fe/HEO@NC layer, the solvated outer sheath can be screened out, promoting faster Li^+ diffusion and participating in the catalytic conversion reaction of LiPSs. As shown in Fig. 2a, in the PP system, the main peak is located at 741 cm^{-1}. However, the peak moves towards contact ion pair (CIP) at 745 cm^{-1} and aggregate (AGG) at 750 cm^{-1} with the introduction of SA-Fe/HEO@NC, indicating a change in the solvation structure of Li^+ [36,37]. Fig. 2b summarizes the result of SA-Fe/HEO@NC system with the highest overall ratio of AGG+CIP (89 %), significantly higher than HEO@NC (76 %), MEO@NC (58 %) and pure PP system (52 %), indicating the rapid dissociation behavior to allow more anions to participate in pairing. The Li^+ transference numbers of the three samples are demonstrated in Fig. 2c. Compared with HEO@NC (0.40) and MEO@NC (0.36), SA-Fe/HEO@NC has the highest transfer number (0.60), indicating the SA-Fe/HEO@NC catalyst enhances the internal diffusion kinetics of Li^+ and the sulfur conversion kinetics. In addition, cyclic voltammetry (CV) measurements, the SA-Fe/HEO@NC cell exhibits the highest peak current and the greatest area, demonstrating better catalytic performance than HEO@NC cell and MEO@NC (Fig. 2d). Fig. 2e displays the self-discharge behavior of the Li-S battery with different catalysts, where the voltage fluctuations before and after resting period can be observed. By magnifying the voltage-time curve, the SA-Fe/HEO@NC cell exhibits more stable voltage and higher voltage values compared to the HEO@NC and MEO@NC cells. Subsequently, as demonstrated in electrochemical impedance spectroscopy (EIS) measurements (**Fig. S6**), [38–40] the charge transfer resistance of SA-Fe/HEO@NC (22.90 Ω) is obviously lower than HEO@NC (39.58 Ω) and MEO@NC (81.39 Ω) (**Table S1**), meaning fast charge transfer and conducive to the transformation of LiPSs. As observed in **Fig. S7**, compared to the cells with HEO@NC (91.61 kJ/mol) and MEO@NC (118.64 kJ/mol), the reaction energy barrier for the cell with SA-Fe/HEO@NC (81.90 kJ/mol) is significantly lower, indicating that SA-Fe/HEO@NC effectively accelerates Li^+ transport and enhances reaction kinetics [41]. In addition, potentiostatic discharge measurements are performed to verify the effectiveness of SA-Fe/HEO@NC in regulating the Li_2S nucleation. As shown in Figs. 2f and **S8**, the current response time of SA-Fe/HEO@NC is 303 s, which is considerably lower than that of HEO@NC (799 s) and MEO@NC (1060 s). Moreover, the precipitation capacity of SA-Fe/HEO@NC, HEO@NC, and MEO@NC electrodes is determined to be 202.0, 181.6, and 133.5 mAh g^{-1}, respectively, revealing the SA-Fe/HEO@NC exhibits a faster response speed to polysulfides and an excellent catalytic ability in promoting the formation of long-chain polysulfides into Li_2S.

In order to accurately describe the electrocatalytic activity of SA-Fe/HEO@NC, the non-Faraday capacitance current corresponding to the CV curves is tested (**Fig. S9**), further clarifying the electrochemical active surface area (ECSA). The electrochemical double-layer capacitance (C_{dl}) of SA-Fe/HEO@NC is 3.5 mF cm^{-2}, which is higher than the capacitance of HEO@NC (2.5 mF cm^{-2}) and MEO@NC (1.3 mF cm^{-2}) in Fig. 2 g. Moreover, the cell with SA-Fe/HEO@NC exhibits a lower Tafel slope (30.4 mV dec^{-1}) than HEO@NC (74.4 mV dec^{-1}) and MEO@NC (166.1 mV dec^{-1}) (Fig. 2h). Besides, the cell with SA-Fe/HEO@NC also shows a

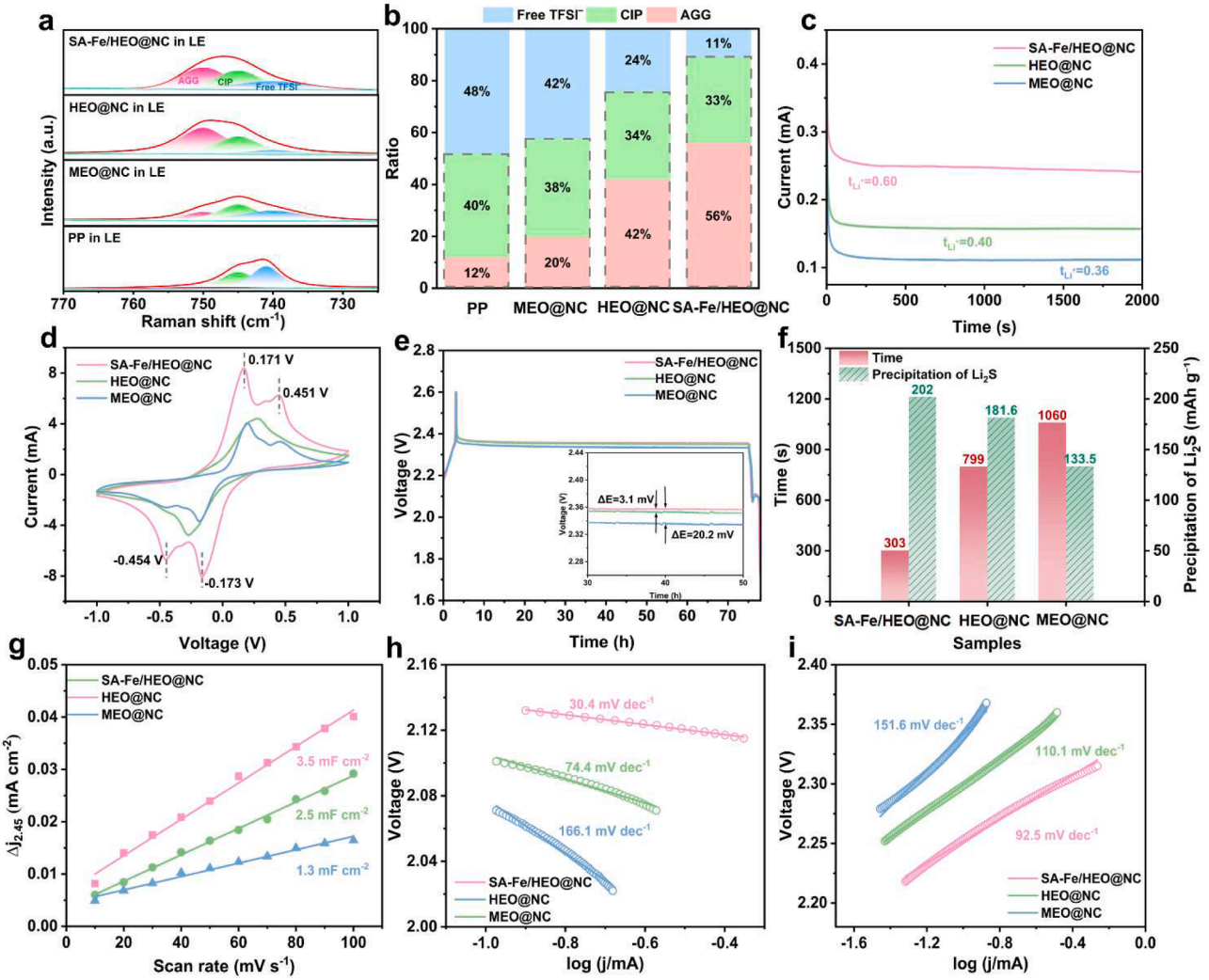

Fig. 2. a) Raman analysis of MEO@NC, HEO@NC and SA-Fe/HEO@NC in the electrolyte, with corresponding b) ratios of solvated $TFSI^-$, CIP and AGG. c) Li^+ transference number under the three systems. d) CV curves. e) Enlarged voltage-time curves of the three batteries during 72 h resting process. f) Comparison of Li_2S deposition peak current and capacity of different samples. g) The capacitive current and scan rate curves. Corresponding Tafel curve calculated by (h, i) reduction and oxidation peaks.

much smaller Tafel slope value (92.5 mV dec ^{1}) compared to HEO@NC (110.1 mV dec ^{1}) and MEO@NC (151.6 mV dec ^{1}) (Fig. 2i) during the oxidation process, indicating a rapid LiPSs conversion kinetics. In addition, the SA-Fe/HEO@NC **(Fig. S10)** reveals the lowest equilibrium polarization voltage of 50 mV (V_1), actual polarization voltage of 170 mV (V_2) and nucleation overpotential of 60 mV (ΔV) in the galvanostatic intermittent titration technique (GITT), confirming the strong electrocatalytic activity of SA-Fe/HEO@NC in L_2S decomposition.

To further explain the electrocatalytic mechanism of SA-Fe/HEO@NC for sulfur conversion, the density of states (DOS) of SA-Fe/HEO@NC, HEO@NC and MEO@NC were calculated (Fig. 3a–c). Fe doping introduces additional electronic states, increasing the density of states near the Fermi level, which optimizes the electronic structure of high-entropy oxides and enhances the electron transport efficiency. This optimization of the electronic structure contributes to reducing the diffusion energy barrier of lithium ions, thereby improving the rate capability and cycling stability of Li-S batteries [28]. In addition, the binding energy between SA-Fe/HEO@NC and polysulfides are higher than that of HEO@NC and MEO@NC (Figs. 3d and **S11–13**), implying the implantation of Fe atom to the HEO@NC can significantly enhance its adsorption with LiPSs owing to the high electronegativity of Fe atom. Fig. 3e shows the Gibbs free energy diagram of the reaction from S_8 to Li_2S. The reduction of S_8 to Li_2S_8 on the three substrates is a spontaneous exothermic reaction, while the subsequent liquid-solid nucleation process (Li_2S_6 to Li_2S) is an endothermic reaction. Therefore, the conversion of Li_2S_6 to Li_2S_2 and Li_2S in Li-S battery mainly attributes the slow redox reaction kinetics between sulfur and LiPSs. As shown in **Fig. S14**, the decomposition energy barrier of Li_2S on SA-Fe/HEO@NC (1.08 eV) is lower than that on HEO@NC (1.55 eV) and MEO@NC (1.71 eV), which demonstrates that the SA-Fe/HEO@NC significantly facilitates the phase transformation of Li_2S during the sulfur reduction reaction process, thereby enhancing the overall electrochemical performance [42–44]. In this regard, the electron density between Li_2S_6 and SA-Fe/HEO@NC (blue and yellow sites in Fig. 3f) is much larger than that between Li_2S_6 and HEO@NC, MEO@NC (blue and yellow sites in Fig. 3 g and 3h), indicating the strong interactions between Li_2S_6 and SA-Fe/HEO@NC. The integration of experimental characterizations and DFT simulations indicates that SA-Fe/HEO@NC markedly reduces the Li^+ desolvation energy barrier, owing to its unique structural design and catalytic strategy. The single-atom Fe optimizes the electronic structure, while the high-entropy oxide matrix ensures stable anchoring sites and abundant active centers. Moreover, the hierarchical pore structure enhances the dissociation of solvated Li^+ via a size-sieving effect and propels Li^+ transport. The cooperative effects of these factors contribute to

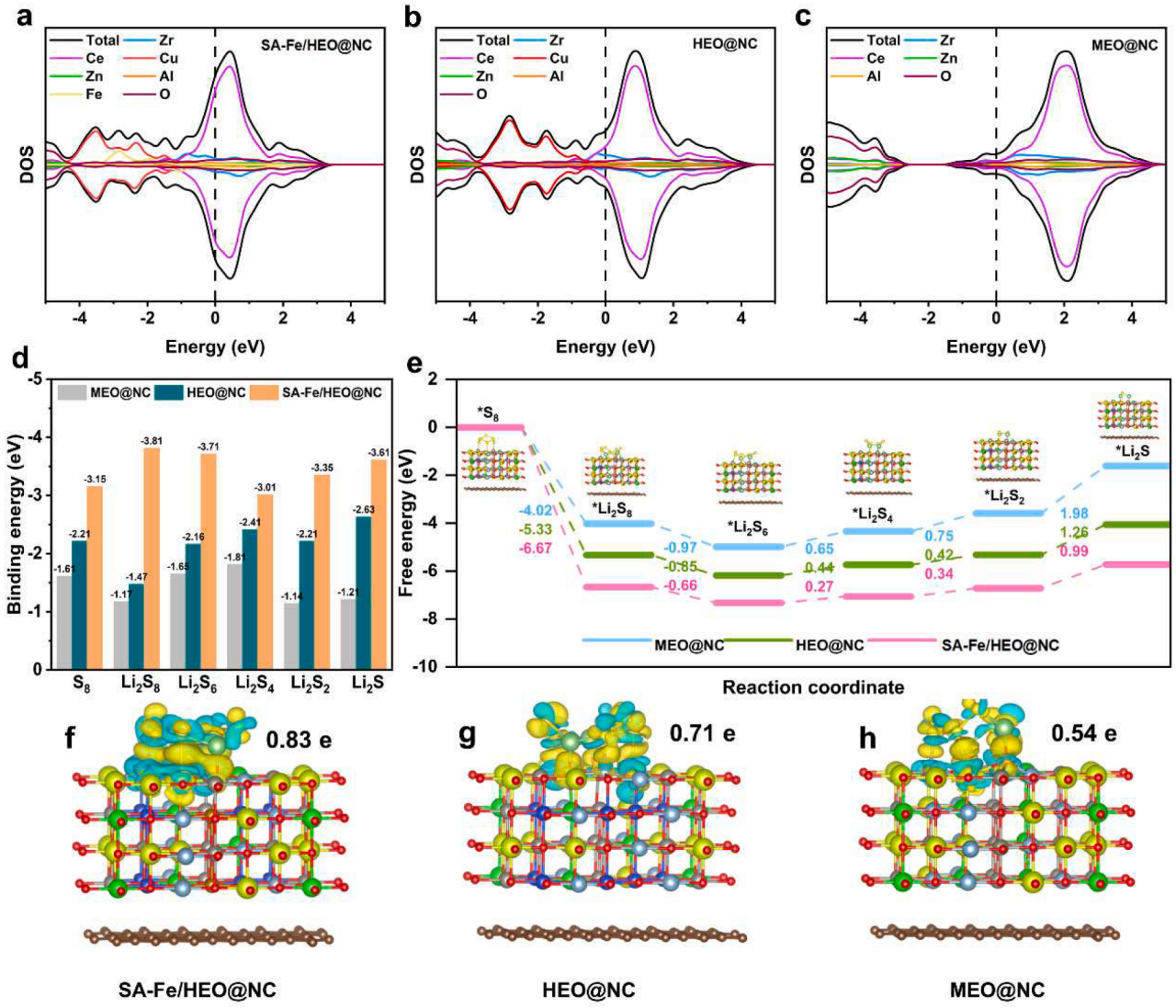

Fig. 3. Calculated density of states of a) SA-Fe/HEO@NC, b) HEO@NC and c) MEO@NC. d) Binding energy of various S species adsorbed on MEO@NC, HEO@NC and SA-Fe/HEO@NC. e) Energy profiles for the reduction of polysulfides and decomposition of the Li_2S cluster on MEO@NC, HEO@NC and SA-Fe/HEO@NC. The charge densities for Li_2S_6 adsorbed on f) SA-Fe/HEO@NC, g) HEO@NC and h) MEO@NC.

the outstanding electrochemical performance of SA-Fe/HEO@NC in Li-S batteries.

In order to further investigate the effect of polysulfide conversion kinetics of the three catalysts on their electrochemical performance, as shown in **Fig. S15a–c**, the two reduction peaks at approximately 2.01(II) and 2.26 V(III) correspond to the reduction of S_8 to soluble polysulfides and the further conversion of polysulfides to Li_2S. By calculation, the SA-Fe/HEO@NC cell has the highest slope, and the slopes corresponding to peak I, peak II and peak III are 160.70, 79.82 and 60.68 (**Fig. S15d–f**), which are higher than HEO@NC (123.08, 58.64, 48.10) and MEO@NC (113.92, 48.53, 29.89), indicating SA-Fe/HEO@NC could accelerate the conversion of soluble polysulfides to Li_2S_2/Li_2S. To find the implicit information reflecting the dynamic behavior, we conduct a self-discharge test and study the charge/discharge curves at 0.2 C (Fig. 4a). During the liquid-liquid (Li_2S_8-Li_2S_4) phase transition, the capacity (Q_1) of the SA-Fe/HEO@NC cell is 364 mAh g^{-1}, which is higher than that of HEO@NC and MEO@NC cells. During the deposition and growth of Li_2S on the second platform, SA-Fe/HEO@NC provides the maximum capacity of 900 mAh g^{-1} (Q_2) and Q_2/Q_1 value of 2.4 (**Fig. S16**), reflecting an efficient Li_2S_4-Li_2S conversion. The minimum platform gap ΔE (0.78 V) and longest discharge platform are observed on SA-Fe/HEO@NC, indicating their superior ability to rapidly convert LiPS into Li_2S. The initial capacity of the SA-Fe/HEO@NC battery showcase the highest capacity of 1262 mAh g^{-1} at 0.2 C and preserves at 1035 mAh g^{-1} after 100 cycles (Fig. 4b), superior to those of reported Li-S batteries (**Table S2**). On the contrary, the batteries with HEO@NC and MEO@NC only maintain 900 and 817 mAh g^{-1} after 100 cycles, respectively. As shown in Figs. 4c and **S17**, the specific capacities of the cell with SA-Fe/HEO@NC are 1289, 1021, 929, 791 and 673 mAh g^{-1} at 0.2, 0.5, 1, 2 and 3 C, respectively, superior to that of HEO@NC and MEO@NC. When the current density is restored to 0.5 C, the capacity recovers to 1017 mAh g^{-1}, demonstrating excellent reversibility. Furthermore, even increasing to 5.8 mg cm^{-2}, the initial capacity of the cells is 6.9 mAh cm^{-2} and retains 4.1 mAh cm^{-2} at 0.1 C (Fig. 4d) after 200 cycles. Moreover, the high sulfur loading cathode with SA-Fe/HEO@NC still provide 2.4 mAh cm^{-2} at 1 C after 200 cycles. The main reasons for capacity degradation in Li-S batteries are the shuttle effect of LiPSs and the corrosion of the Li anode. Impressively, the cell with SA-Fe/HEO@NC exhibits excellent long-term cycling stability at 1 C, with a capacity decay of only 0.048 % per cycle over 1000 cycles (Fig. 4e). This remarkable stability can be attributed to the synergistic effects of the single-atom Fe catalyst and the high-entropy oxide matrix,

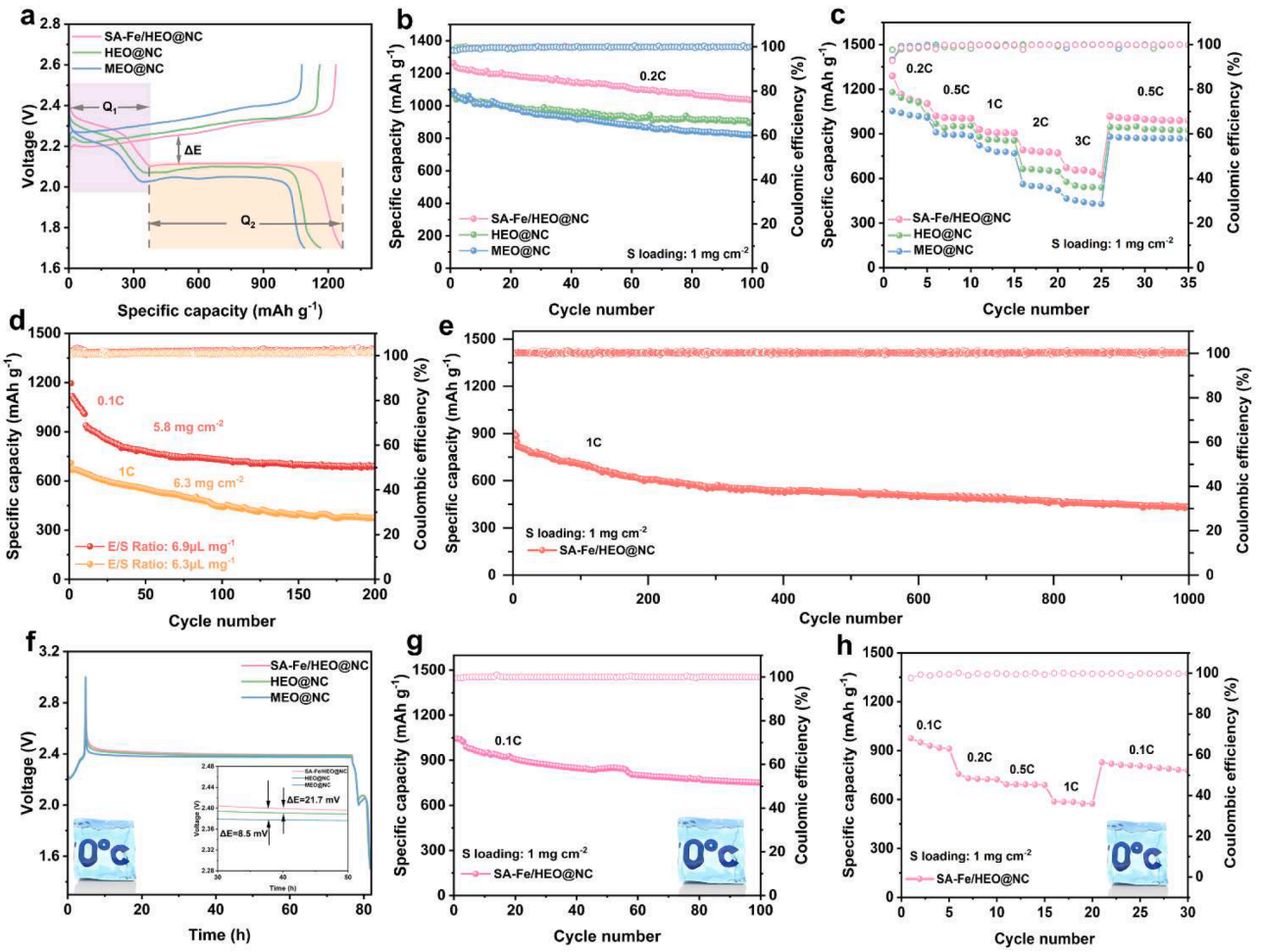

Fig. 4. a) Voltage curves. b) Comparison of cycle performance at 0.2 C. c). Rate performance of SA-Fe/HEO@NC, HEO@NC and MEO@NC modified cells. d) Cycling performance of Li-S cells with SA-Fe/HEO@NC modified separators under a high sulfur loading of 5.8 mg cm^{-2} at 0.1 C and 6.3 mg cm^{-2} at 1 C. e) Long cycling performance of the Li-S battery with SA-Fe/HEO@NC modified separator at 1 C. f) Enlarged voltage-time curves of the three batteries during 72 h standing process under harsh conditions of 0 °C. g) Cyclic performance of SA-Fe/HEO@NC modified cell at 0.1 C under harsh conditions of 0 °C. h) Rate performance of SA-Fe/HEO@NC modified cell under harsh conditions of 0 °C.

which synergistically enhances the structural integrity and catalytic efficiency of the electrode. The low decay rate suggests that the Fe single atoms effectively catalyze the conversion of LiPSs, thereby inhibiting the shuttle effect. Considering the impact of ion diffusion kinetics in harsh environments, such as low-temperature, the performance of SA-Fe/HEO@NC battery is measured at 0 °C, showing enhanced performance compared to that of reported Li-S batteries (**Table S3**). By magnifying the voltage-time curve during the 72 h resting period (Fig. 4f), the SA-Fe/HEO@NC based battery exhibited more stable voltage performance and higher voltage values. The discharge capacity of the SA-Fe/HEO@NC based battery decreases from 989 mAh g^{-1} to 751 mAh g^{-1} with a high-capacity retention rate of 75.9 % after 100 cycles, demonstrating excellent cycle stability at low temperatures (Fig. 4 g). As shown in **Fig. S18**, the SA-Fe/HEO@NC, HEO@NC, and MEO@NC cells all exhibit two distinct voltage plateaus at 0 °C. It can be observed that compared to the HEO@NC and MEO@NC cells, the SA-Fe/HEO@NC cell demonstrates enhanced capacities for both the high-voltage plateau (Q_2) and the low-voltage plateau (Q_1), particularly for the low-voltage plateau. This indicates that the presence of SA-Fe/HEO@NC positively promotes the reduction of soluble intermediate LiPSs to Li_2S, even at low temperatures, thereby improving the utilization efficiency of the active sulfur material. The rate performance of SA-Fe/HEO@NC based battery is also measured at a low temperature under 0 °C (Fig. 4h), delivering a capacity of 588 mAh g^{-1} at 1 C. As the rate reduced to 0.1 C, the capacity is restored to 809 mAh g^{-1}. These results strongly prove that SA-Fe/HEO@NC can well promote the release and migration of Li^+ at low temperatures, thereby inhibiting the dissolution and shuttle of intermediates in the electrolyte, and facilitating the oxidation/reduction reaction of sulfur species.

In situ Raman spectroscopy is used to study the transformation mechanism of polysulfides during charge and discharge. For pristine PP (Fig. 5a and 5b), at the beginning of the discharge process (about 2.4 V), two characteristic peaks belonging to Li_2S_8 appear at 150 and 471 cm^{-1} [45]. As the discharge continued, peaks for Li_2S_4 and Li_2S_6 (218 and 397 cm^{-1}) begin to appear, indicating severe "shuttle effect" occurred. At the end of discharge state (1.72 V), most of the characteristic peaks decreases rapidly except the peak of electrolyte at 471 cm^{-1} [5]. In contrast, SA-Fe/HEO@NC based battery shows almost no characteristic peaks of polysulfides during discharge process (Fig. 5c and 5d), demonstrating the polysulfide is effectively confined to cathode due to the excellent adsorption and catalytic properties of SA-Fe/HEO@NC. Time-of-flight secondary ion mass spectrometry (ToF-SIMS) further confirmed the binding and catalytic effects of SA-Fe/HEO@NC on polysulfides. Fig. 5e shows that S , LiS and total ions in the selected region of the cycled sulfur cathode at 0.2 C with SA-Fe/HEO@NC functional separator are weaker than MEO@NC, indicating less sulfur aggregation on the cathode surface of the SA-Fe/HEO@NC system. In addition, the 3D images (Fig. 5f) shows that more S and Li^+ secondary ion species are

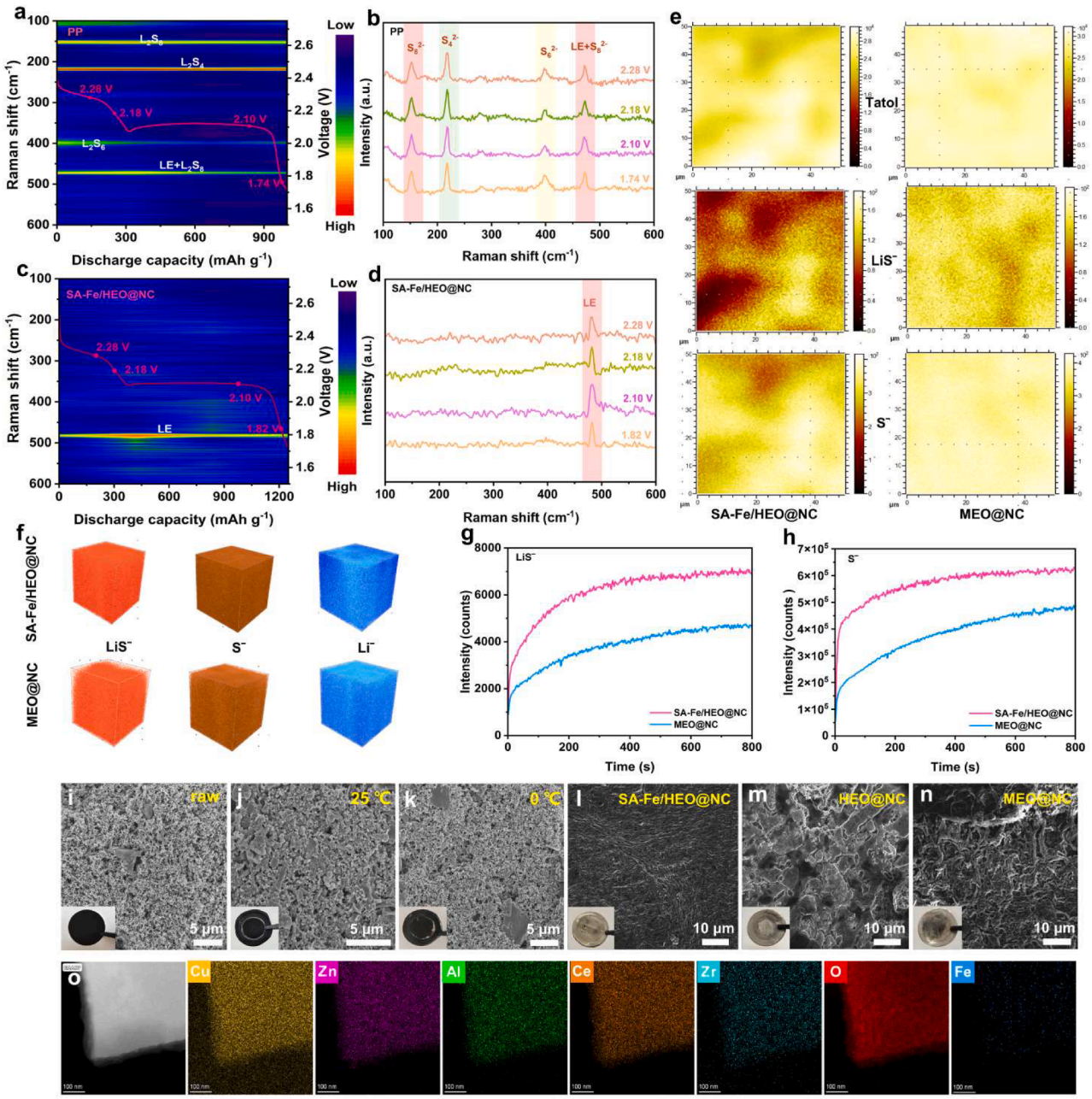

Fig. 5. (a, c) PP and SA-Fe/HEO@NC/PP in the time-resolved Raman spectra during the discharge process and the corresponding discharge curves, as well as the selected (b, d) Raman spectra. e) ToF-SIMS total, LiS^- and S^- mappings on the top surfaces of the KB/S cathodes with SA-Fe/HEO@NC/PP and MEO@NC/PP. f) 3D rendering secondary ions depth profile images of the cycled cells with SA-Fe/HEO@NC and MEO@NC. ToF-SIMS g) LiS^- and h) S^- depth profile images of the cycled anodes. SEM image of SA-Fe/HEO@NC i) before cycling. j) After 100 cycles at room temperature at 0.2 C. k) After 100 cycles at 0.1 C under harsh conditions of 0 °C. l–n) SEM images of lithium of SA-Fe/HEO@NC, HEO@NC and MEO@NC. o) Mapping of SA-Fe/HEO@NC modified separators after cycling.

confined and evenly distributed in the cathode of the SA-Fe/HEO@NC system, consistent with the depth distribution in Fig. 5e. The cell with SA-Fe/HEO@NC (Fig. 5 g and 5h) exhibits higher intensities at the beginning and final periods, suggesting that the SA-Fe/HEO@NC is able to inhibit polysulfide aggregation. To further explore the cycling stability of SA-Fe/HEO@NC catalyst, the morphology of the SA-Fe/HEO@NC modified separator after cycles at room (Fig. 5j) and low temperatures (Fig. 5k) is studied. Compared with pristine separator (Fig. 5i), the SA-Fe/HEO@NC separator retains similar morphology with almost no changes after cycling at either room temperature or low temperatures. Besides, the Li anode in the SA-Fe/HEO@NC system also exhibits a uniform morphology with no chaotic deposition of Li_2S and no obvious dendrite growth (Fig. 5l). In contrast, disordered Li_2S deposition and Li dendrites appear in the HEO@NC (Fig. 5m) and MEO@NC (Fig. 5n) systems. This result indicates that SA-Fe/HEO@NC contributes to inhibit the shuttle of LiPSs and promote the catalytic conversion of LiPSs [46–49]. In addition, the SA-Fe/HEO@NC modified separator after circulation is also characterized by SEM and EDS (Fig. 5o). The uniform distribution of Cu, Zn, Al, Ce, Zr, O and Fe can be observed, which further proves the stability of the SA-Fe/HEO@NC coating layer during the cycle. To further investigate the surface composition of cycled cathodes, XPS analysis was performed. As shown in the C 1 s spectra (**Fig. S19a**), compared to MEO@NC, SA-Fe/HEO@NC exhibits distinct negative shifts in the characteristic peaks corresponding to C–C/C=C (284.8 eV), C–S (286.5 eV), C=O (289.9 eV), and C–F (292.8 eV) [50]. Similar peak shifts were observed in the S 2p (**Fig. S19b**) and

Li 1 s spectra (**Fig. S19c**) for SA-Fe/HEO@NC. These results indicate that the enhanced chemical adsorption capability of SA-Fe/HEO@NC toward polysulfides effectively suppresses the shuttle effect. Compared with the pristine Fe single atoms (Fig. 1i), the X-ray photoelectron spectroscopy (XPS) peaks of Fe single atoms exhibited negligible variation after charge/discharge cycles (**Fig. S20**), indicating their persistent functionality as catalytic active centers to facilitate LiPSs conversion throughout electrochemical processes. This observation further demonstrates that both the adsorption capability and catalytic activity of Fe single atoms toward LiPSs remain stable during cycling, thereby contributing to durable suppression of the shuttle effect and the enhancement cycling stability of the battery.

3. Conclusion

In summary, we successfully synthesize an efficient electrocatalyst composed of high-entropy oxides with atomically dispersed iron supported on a porous carbon matrix (SA-Fe/HEO@NC). This catalyst facilitates the desolvation of Li^+, resulting in the release of free Li^+ and enhancing the redox kinetics of sulfur conversion. Through spectral and electrochemical tests and theoretical simulations, the introduction of Fe single atoms can directly regulate the electronic structure of high-entropy oxides, while high-entropy oxides containing multiple metal elements provide electrocatalytic sites in the dissociation solvation sheath to facilitate the rapid transport of Li^+. Consequently, the SA-Fe/HEO@NC modified separator shows excellent electrochemical performance (1035 mAh g^{-1} after 100 cycles at 0.2 C). After 200 cycles, the sulfur cathode with ~6 mg cm^{-2} still exhibits an area capacity of 4.1 mAh cm^{-2} at 0.1 C. More importantly, low temperature (0 °C) tests revealed a stable cycle capacity at 0.1 C (751 mAh g^{-1} after 100 cycles) and excellent rate performance (588 mAh g^{-1} at 1 C), suggesting the potential of atomic catalyst on high-entropy oxide for high-performance Li-S batteries.

CRediT authorship contribution statement

Fei Na: Writing – original draft, Data curation, Conceptualization. **Xiang Li:** Investigation, Formal analysis. **Jian Wang:** Writing – review & editing. **Xiaomin Cheng:** Methodology, Investigation. **Jing Zhang:** Resources, Funding acquisition. **Yanli Wang:** Resources, Funding acquisition. **Hongzhen Lin:** Software, Resources. **Liang Zhan:** Resources, Funding acquisition. **Licheng Ling:** Software, Resources, Funding acquisition. **Yongzheng Zhang:** Writing – review & editing, Funding acquisition, Conceptualization.

Declaration of competing interest

The authors declare that they have no known competing financial interests or personal relationships that could have appeared to influence the work reported in this paper.

Acknowledgements

This work is supported by the funding from the National Natural Science Foundation of China (52372045, 22075081, 22279161, 22309144, and U1710252), National Key R&D Program of China (2021YFA1201503), Shanghai Sailing Program of China (23YF1408900), Natural Science Foundation of Jiangsu Province (BK. 20210130), China Postdoctoral Science Foundation (2023M731084, 2024M762318) as well as the Opening funding from Key Laboratory of Engineering Dielectrics and Its Application (Harbin University of Science and Technology) (No. KFM202507, Ministry of Education) are acknowledged. The author thanks the scientific support from Nano-X, Suzhou Institute of Nano-Tech and Nano-Bionics, Chinese Academy of Sciences.

Data availability

Data will be made available on request.

References

[1] F. Han, Z. Wang, Q. Jin, L. Fan, K. Tao, L. Li, L. Shi, H.Q. Lu, Z. Zhang, J. Li, X. Zhang, L. Wu, High-entropy alloy electrocatalysts bidirectionally promote lithium polysulfide conversions for long-cycle-life lithium-sulfur batteries, ACS Nano 18 (2024) 15167–15176.
[2] J. Zhang, C. You, H. Lin, J. Wang, Electrochemical kinetic modulators in lithium–sulfur batteries: from defect-rich catalysts to single atomic catalysts, Energy Environ. Mater. 5 (2022) 731–750.
[3] X. Li, Y. Zuo, Y. Zhang, J. Wang, Y. Wang, H. Yu, L. Zhan, L. Ling, Z. Du, S. Yang, Controllable sulfurization of mxenes to in-plane multi-heterostructures for efficient sulfur redox kinetics, Adv. Energy Mater. 14 (2024) 2303389.
[4] Y. Li, Y. Zuo, X. Li, Y. Zhang, C. Ma, X. Cheng, J. Wang, J. Wang, H. Lin, L. Ling, Electron delocalization-enhanced sulfur reduction kinetics on an MXene-derived heterostructured electrocatalyst, Nano Res. 17 (2024) 7153–7162.
[5] X. Li, Q. Guan, Z. Zhuang, Y. Zhang, Y. Lin, J. Wang, C. Shen, H. Lin, Y. Wang, L. Zhan, L. Ling, Ordered mesoporous carbon grafted MXene catalytic heterostructure as Li-ion kinetic pump toward high-efficient sulfur/sulfide conversions for Li-S battery, ACS Nano 17 (2023) 1653–1662.
[6] C. Ye, H. Li, Y. Chen, J. Hao, J. Liu, J. Shan, S.Z. Qiao, The role of electrocatalytic materials for developing post-lithium metal||sulfur batteries, Nat. Commun. 15 (2024) 4797.
[7] C. Dong, C. Ma, C. Zhou, Y. Yu, J. Wang, K. Yu, C. Shen, J. Gu, K. Yan, A. Zheng, M. Gong, X. Xu, L. Mai, Engineering d-p orbital hybridization with P, S co-coordination asymmetric configuration of single atoms toward high-rate and long-cycling lithium-sulfur battery, Adv. Mater. 36 (2024) 2407070.
[8] J. Wang, J. Zhang, Y. Zhang, H. Li, P. Chen, C. You, M. Liu, H. Lin, S. Passerini, Atom-level tandem catalysis in lithium metal batteries, Adv. Mater. 36 (2024) 2402792.
[9] J. Wang, J. Zhang, J. Wu, M. Huang, L. Jia, L. Li, Y. Zhang, H. Hu, F. Liu, Q. Guan, M. Liu, H. Adenusi, H. Lin, S. Passerini, Interfacial "Single-Atom-in-Defects" catalysts accelerating Li^+ desolvation kinetics for long-lifespan lithium-metal batteries, Adv. Mater. 35 (2023) 2302828.
[10] J. Wang, L. Jia, S. Duan, H. Liu, Q. Xiao, T. Li, H. Fan, K. Feng, J. Yang, Q. Wang, M. Liu, J. Zhong, W. Duan, H. Lin, Y. Zhang, Single atomic cobalt catalyst significantly accelerates lithium-ion diffusion in high mass loading Li_2S cathode, Energy Storage Mater. 28 (2020) 375–382.
[11] L. Huang, J. Zhu, J.X. Liu, H. Wu, G.J. Zhang, Emerging high-entropy strategy: a booster to the development of cathode materials for power batteries, J. Adv. Ceram. 13 (2024) 1093–1118.
[12] M. Tamtaji, M.G. Kim, J. Wang, P.R. Galligan, H. Zhu, F.F. Hung, Z. Xu, Y. Zhu, Z. Luo, W.A. Goddard, G. Chen, A high-entropy single-atom catalyst toward oxygen reduction reaction in acidic and alkaline conditions, Adv. Sci. 11 (2024) 2309883.
[13] B. Wang, Q. Wang, B. Sun, J. Mo, Y. Guo, X. Liang, B. Shen, Nitride-reinforced HfNbTaTiV high-entropy alloy with excellent room and elevated-temperature mechanical properties, J. Mater. Sci. Technol. 149 (2023) 31–41.
[14] X.L. Wang, E.M. Kim, T.G. Senthamaraikannan, D.H. Lim, S.M. Jeong, Porous hollow high entropy metal oxides $(NiCoCuFeMg)_3O_4$ nanofiber anode for high-performance lithium-ion batteries, Chem. Eng. J. 484 (2024) 149509.
[15] X. Li, W. Zhang, K. Lv, J. Liu, A. Bayaguud, Research progress on high-entropy oxides as advanced anode, cathode, and solid-electrolyte materials for lithium-ion batteries, J. Power Sources 620 (2024) 235259.
[16] H. Xu, R. Hu, Y. Zhang, H. Yan, Q. Zhu, J. Shang, S. Yang, B. Li, Nano high-entropy alloy with strong affinity driving fast polysulfide conversion towards stable lithium sulfur batteries, Energy Storage Mater. 43 (2021) 212–220.
[17] H. Wang, Y. Shi, M. Li, Y. Ye, Y. Zhang, T. Rong, Z. Wang, J. Zhang, H. Chen, Y. Tao, Q. Zhao, J. Gu, F. Ye, L. Mai, Z. Du, S. Yang, High-entropy 1T-phase quantum sheets of transition-metal disulfides, Adv. Mater. (2025) 2500321.
[18] Y.C. Lin, Y.H. Wu, J.M. Ting, S.H. Chung, Stable lithium–sulfur cell separator with a high-entropy metal oxide modification, Energy Fuels 37 (2023) 15162–15169.
[19] X. Wang, P. Lin, C. Wu, Y. Zhu, C. Wang, D. Guo, X.A. Chen, S. Wang, Superior-performance lithium–sulfur batteries: a face-centered-cubic-structure high-entropy alloy improves the bidirectional catalytic conversion of polysulfides/sulfides, Inorg. Chem. Front. 11 (2024) 6425–6437.
[20] L. He, M. Li, L. Qiu, S. Geng, Y. Liu, F. Tian, M. Luo, H. Liu, Y. Yu, W. Yang, S. Guo, Single-atom Mo-tailored high-entropy-alloy ultrathin nanosheets with intrinsic tensile strain enhance electrocatalysis, Nat. Commun. 15 (2024) 2290.
[21] Y. Cui, Y. Zhang, Z. Cao, J. Gu, Z. Du, B. Li, S. Yang, A perspective on high-entropy two-dimensional materials, SusMat 2 (2022) 65–75.
[22] K.C. Pitike, A. Macias, M. Eisenbach, C.A. Bridges, V.R. Cooper, Computationally accelerated discovery of high entropy pyrochlore oxides, Chem. Mater. 34 (2022) 1459–1472.

[23] L. Spiridigliozzi, C. Ferone, R. Cioffi, G. Dell'Agli, A simple and effective predictor to design novel fluorite-structured High Entropy Oxides (HEOs), Acta Mater. 202 (2021) 181–189.

[24] A. Sarkar, P.K. Mannava, L. Velasco, C. Das, B. Breitung, S.S. Bhattacharya, R. Kruk, H. Hahn, Determining role of individual cations in high entropy oxides: structure and reversible tuning of optical properties, Scr. Mater. 207 (2022) 114273.

[25] S. Li, Z. Peng, X. Fu, $Zn_{0.5}Co_{0.5}Mn_{0.5}Fe_{0.5}Al_{0.5}Mg_{0.5}O_4$ high-entropy oxide with high capacity and ultra-long life for Li-ion battery anodes, J. Adv. Ceram. 12 (2023) 59–71.

[26] J. Gu, Y. Zhang, Y. Shi, Y. Jin, H. Chen, X. Sun, Y. Wang, L. Zhan, Z. Du, S. Yang, M. Li, Heteroatom immobilization engineering toward high-performance metal anodes, ACS Nano 18 (2024) 25966–25985.

[27] P. Chen, T. Huang, T. Wei, B. Ding, H. Dou, X. Zhang, Enhanced transformation kinetics of polysulfides enabled by synergistic catalysis of functional graphitic carbon nitride for high-performance Li-S batteries, Adv. Funct. Mater. (2024) 2420351.

[28] D. Zhang, S. Wang, R. Hu, J. Gu, Y. Cui, B. Li, W. Chen, C. Liu, J. Shang, S. Yang, Catalytic conversion of polysulfides on single atom zinc implanted mxene toward high-rate lithium–sulfur batteries, Adv. Funct. Mater. 30 (2020) 2002471.

[29] Y. Liu, C. Lu, Y. Yang, W. Chen, F. Ye, H. Dong, Y. Wu, R. Ma, L. Hu, Multiple cations nanoconfinement in ultrathin V_2O_5 nanosheets enables ultrafast ion diffusion kinetics toward high-performance zinc ion battery, Adv. Mater. 36 (2024) 2312982.

[30] D. Wang, Z. Liu, S. Du, Y. Zhang, H. Li, Z. Xiao, W. Chen, R. Chen, Y. Wang, Y. Zou, S. Wang, Low-temperature synthesis of small-sized high-entropy oxides for water oxidation, J. Mater. Chem. A 7 (2019) 24211–24216.

[31] L. Yang, Y. Pan, Z. Zhou, Y. Zhang, J. Xu, C. Ma, Y. Zhang, J. Wang, W. Qiao, L. Ling, Vanadium as auxiliary for Fe-V dual-atom electrocatalyst in lithium–sulfur batteries: "3D in 2D" morphology inducer and coordination structure regulator, ACS Nano 17 (2023) 17405–17416.

[32] J. Xu, S. Zhang, H. Liu, S. Liu, Y. Yuan, Y. Meng, M. Wang, C. Shen, Q. Peng, J. Chen, X. Wang, L. Song, K. Li, W. Chen, Breaking local charge symmetry of iron single atoms for efficient electrocatalytic nitrate reduction to ammonia, Angew. Chem. Int. Ed. 62 (2023) e202308044.

[33] W. Wang, W. Song, Y. Li, Y. Guo, K. Yang, L. Yu, F. Xie, Q. Ren, K. He, S. Wang, Y. Yuan, Mesocrystallinely stabilized lithium storage in high-entropy oxides, Nano Energy 124 (2024) 109482.

[34] L. Ren, J. Liu, Y. Zhao, Y. Wang, X. Lu, M. Zhou, G. Zhang, W. Liu, H. Xu, X. Sun, Regulating electronic structure of Fe-N_4 single atomic catalyst via neighboring sulfur doping for high performance lithium-sulfur batteries, Adv. Funct. Mater. 33 (2023) 2210509.

[35] X. Zhang, X. Li, Y. Zhang, X. Li, Q. Guan, J. Wang, Z. Zhuang, Q. Zhuang, X. Cheng, H. Liu, J. Zhang, C. Shen, H. Lin, Y. Wang, L. Zhan, L. Ling, Accelerated Li^+ desolvation for diffusion booster enabling low-temperature sulfur redox kinetics via electrocatalytic carbon-grazfted-CoP porous nanosheets, Adv. Funct. Mater. 33 (2023) 2302624.

[36] D. Yu, H. Wang, W. Zhang, H. Dong, Q. Zhu, J. Yang, S. Huang, Unraveling the role of ion-solvent chemistry in stabilizing small-molecule organic cathode for potassium-ion batteries, Energy Storage Mater. 43 (2021) 172–181.

[37] W. Luo, D. Yu, T. Ge, J. Yang, S. Dong, H. Chen, L. Qin, Y. Huang, D. Chen, Balancing salt concentration and fluorinated cosolvent for graphite cathode-based dual-ion batteries, Appl. Energy 358 (2024) 122652.

[38] L. Peng, Z. Wei, C. Wan, J. Li, Z. Chen, D. Zhu, D. Baumann, H. Liu, C.S. Allen, X. Xu, A.I. Kirkland, I. Shakir, Z. Almutairi, S. Tolbert, B. Dunn, Y. Huang, P. Sautet, X. Duan, A fundamental look at electrocatalytic sulfur reduction reaction, Nat. Catal. 3 (2020) 762–770.

[39] Z. Wu, F. Ye, Q. Liu, R. Pang, Y. Liu, L. Jiang, Z. Tang, L. Hu, Simultaneous incorporation of V and Mn element into polyanionic NASICON for high energy-density and long-lifespan Zn-ion storage, Adv. Energy Mater. 12 (2022) 2200654.

[40] Y. Ma, T. Wu, Y. Jiao, F. Wang, B. Chen, Y. Yan, A. Hu, Y. Li, Y. Fan, M. He, Y. Hu, Y. Li, T. Lei, Y. Zhang, W. Chen, M. Huang, J. Zhu, F. Li, Single nickel atom catalysts enable fast polysulfide redox for safe and long-cycle lithium-sulfur batteries, Small 18 (2022) 2270281.

[41] T. You, H. Sun, W. Hua, S. Geng, Z. Hu, Y. Shang, Q. Huang, S. Dai, K. Chen, Insights into co-catalytic single-atom-support interactions for boosting sulfur reduction electrocatalysis, Angew. Chem. Int. Ed. (2025) e202425144.

[42] Z. Zhao, Y. Pan, S. Yi, Z. Su, H. Chen, Y. Huang, B. Niu, D. Long, Y. Zhang, Enhanced electron delocalization within coherent nano-heterocrystal ensembles for optimizing polysulfide conversion in high-energy-density Li-S batteries, Adv. Mater. 36 (2024) 2310052.

[43] H. Ding, Z. Chen, H. Li, H. Suo, C. Liu, H. Yu, J. Yuan, Z. Sun, Y. Zhu, B. Song, Regulating Li_2S deposition and accelerating conversion kinetics through intracavity ZnS toward low-temperature lithium–sulfur batteries, Nano Lett. 24 (2024) 15118–15126.

[44] R. Razaq, M.M. Din, D. Småbråten, V. Eyupoglu, S. Janakiram, T. Sunde, N. Allahgoli, D. Rettenwander, L. Deng, Synergistic effect of bimetallic MOF modified separator for long cycle life lithium-sulfur batteries, Adv. Energy Mater. 14 (2023) 2302897.

[45] W. Zhang, J. Zhu, Y. Ye, J. She, X. Kong, S. Jin, Z. Peng, H. Ji, Suppressing shuttle effect via cobalt phthalocyanine mediated dissociation of lithium polysulfides for enhanced Li-S battery performance, Adv. Funct. Mater. 34 (2024) 2403888.

[46] Y. Li, S. Lin, D. Wang, T. Gao, J. Song, P. Zhou, Z. Xu, Z. Yang, N. Xiao, S. Guo, Single atom array mimic on ultrathin mof nanosheets boosts the safety and life of lithium-sulfur batteries, Adv. Mater. 32 (2020) 1906722.

[47] J. Wang, D. Yu, X. Sun, H. Wang, J. Li, Anodes for low-temperature rechargeable batteries, eScience 4 (2024) 100252.

[48] L. Cheng, Y. Wang, J. Yang, M. Tang, C. Zhang, Q. Zhu, S. Wang, Y. Li, P. Hu, H. Wang, An ultrafast and stable Li-metal battery cycled at -40°C, Adv. Funct. Mater. 33 (2023) 2212349.

[49] H. Wang, D. Yu, C. Kuang, L. Cheng, W. Li, X. Feng, Z. Zhang, X. Zhang, Y. Zhang, Alkali metal anodes for rechargeable batteries, Chem 5 (2019) 313–338.

[50] C. Li, S. Wang, Z. Wang, Z. Li, C. Zhang, Y. Ma, X. Shi, H. Zhang, D. Song, L. Zhang, Investigation on the necessity of low rates activation toward lithium-sulfur batteries, Adv. Funct. Mater. 35 (2025) 2414159.